Article

Moon-forming impactor as a source of Earth's basal mantle anomalies

https://doi.org/10.1038/s41586-023-06589-1

Received: 4 February 2022

Accepted: 30 August 2023

Published online: 1 November 2023

Check for updates

Qian Yuan[1,2]✉, Mingming Li[1], Steven J. Desch[1], Byeongkwan Ko[1,3], Hongping Deng[4], Edward J. Garnero[1], Travis S. J. Gabriel[5], Jacob A. Kegerreis[6], Yoshinori Miyazaki[2], Vincent Eke[7] & Paul D. Asimow[2]

Seismic images of Earth's interior have revealed two continent-sized anomalies with low seismic velocities, known as the large low-velocity provinces (LLVPs), in the lowermost mantle[1]. The LLVPs are often interpreted as intrinsically dense heterogeneities that are compositionally distinct from the surrounding mantle[2]. Here we show that LLVPs may represent buried relics of Theia mantle material (TMM) that was preserved in proto-Earth's mantle after the Moon-forming giant impact[3]. Our canonical giant-impact simulations show that a fraction of Theia's mantle could have been delivered to proto-Earth's solid lower mantle. We find that TMM is intrinsically 2.0–3.5% denser than proto-Earth's mantle based on models of Theia's mantle and the observed higher FeO content of the Moon. Our mantle convection models show that dense TMM blobs with a size of tens of kilometres after the impact can later sink and accumulate into LLVP-like thermochemical piles atop Earth's core and survive to the present day. The LLVPs may, thus, be a natural consequence of the Moon-forming giant impact. Because giant impacts are common at the end stages of planet accretion, similar mantle heterogeneities caused by impacts may also exist in the interiors of other planetary bodies.

Terrestrial planet formation concludes with a number of giant impacts among Moon- and Mars-sized planetary embryos[4]. The well-studied giant-impact scenario involves a protoplanet, Theia, colliding with proto-Earth. Earth's Moon subsequently formed from orbitally bound impact debris[5]. Although it is challenging to reconcile the observed lunar isotopes and volatiles[6,7] with the giant-impact hypothesis[3], this Moon-formation hypothesis accounts for several key features of the Earth–Moon system, including the current angular momentum, the Moon's small core and the high mass of the Moon compared with the Earth[3,5]. However, direct evidence for the existence of Theia remains elusive. Here, we demonstrate that a fraction of Theia mantle material (TMM) could have entered the largely solid lower layer of the post-impact Earth's mantle during the canonical Moon-forming impact. This mostly molten TMM could later have solidified and sunk to Earth's lowermost mantle and now constitute the seismically observed large low-velocity provinces (LLVPs)[1] in the present day (Fig. 1).

Previous hypotheses for the origin of the LLVPs, such as remnants of Earth's early differentiation[2,8] and accumulations of subducted oceanic crust[9], specifically involve Earth's internal processes after the Moon-forming giant impact. However, lines of evidence suggest that the LLVPs preserve primordial volatiles that predate the giant impact[10,11], and these volatiles cannot easily be explained by Earth's ensuing differentiation after the Moon's formation. Since Theia predates the Moon, its mantle may have been able to retain nebular gases[12] that were captured due to its large mass before the dissipation of its protoplanetary disc[13]. Thus, a TMM-origin of the LLVPs may explain the presence of nebular components in some ocean-island basalts (OIBs)[11] that are caused by mantle plumes that entrain materials from the LLVPs[14]. This mechanism can also explain the similarity of noble-gas isotopic ratios between OIBs and lunar mare basalts[15]. However, several additional physical and chemical criteria must be met for TMM to be the origin of LLVPs. In what follows, we combine evidence from hydrodynamic simulations of the Moon-forming giant impact, thermal evolution modelling and mantle convection simulations to show the following. (1) The giant impact could have produced a two-layer structure in the Earth's mantle, with an upper molten layer and a lower solid layer. (2) The solid lower layer could have directly incorporated some mostly molten TMM. (3) This molten TMM could solidify, sink and accumulate at the Earth's core–mantle boundary (CMB). (4) Accumulations of TMM on the CMB could survive more than 4.5 billion years without being advected or eroded away from the CMB. (5) The volume and seismic properties of the TMM accumulations are consistent with those of the LLVPs.

We investigated the dynamics and thermal state of Earth's mantle and the TMM during the giant impact using two different hydrodynamical simulation methods with the latest equations of state[16] and at unprecedentedly high resolution[17]. Using a meshless finite mass (MFM) method[18], recent work[19] has shown that a Moon-forming giant impact could lead to a stratified Earth mantle characterized by a compositional change and entropy jump near a depth of approximately

[1]School of Earth and Space Exploration, Arizona State University, Tempe, AZ, USA. [2]Division of Geological and Planetary Sciences, California Institute of Technology, Pasadena, CA, USA. [3]Department of Earth and Environmental Sciences, Michigan State University, East Lansing, MI, USA. [4]Shanghai Astronomical Observatory, Chinese Academy of Sciences, Shanghai, China. [5]U.S. Geological Survey, Astrogeology Science Center, Flagstaff, AZ, USA. [6]NASA Ames Research Center, Moffett Field, CA, USA. [7]Institute for Computational Cosmology, Department of Physics, Durham University, Durham, UK. ✉e-mail: qyuan@caltech.edu

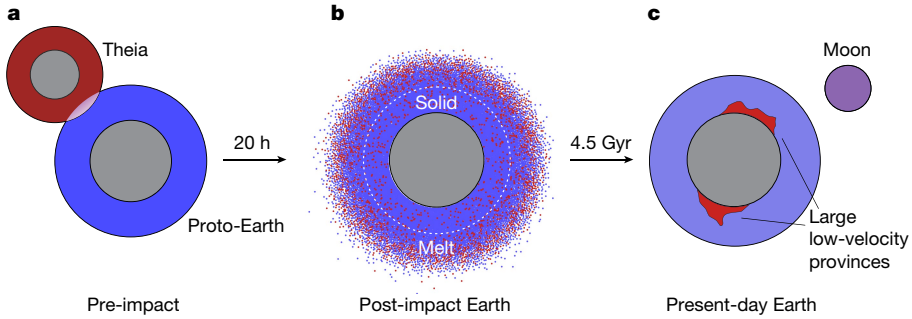

Fig. 1 | Schematic diagram illustrating the giant-impact origin of the LLVPs. **a**, Pre-impact: Theia collides with the proto-Earth. **b**, Post-impact: a stratified mantle forms in the Earth. There is a boundary at a depth of approximately 1,400 km within the present-day mantle (marked by the dashed white line). The mantle of post-impact Earth (blue) below the boundary is largely solid, in contrast with its molten upper layer. Most of the TMM (red) is incorporated in this upper layer, but a portion of the TMM enters the lower layer. Data and stratification model from ref. 19. **c**, Present day: after approximately 4.5 Gyr, the TMM in the lower layer sinks to the CMB and is shaped into two thermochemical piles that represent the LLVPs. The rest of the TMM in the upper layer undergoes significant mixing with the Earth's mantle, which is compositionally similar to the protolunar disc that formed the Moon. The relative sizes of the Earth and Moon and the distance between them are not to scale in **c**.

1,300 km (referenced to Earth's present-day surface radius). From these results[19], we found that a significant amount of TMM, 0.017–0.026 Earth masses ($M_\oplus$) (Extended Data Table 1), could have entered the lower mantle layer, which is comparable with mass estimates of approximately 0.01–0.06 $M_\oplus$ for the LLVPs[14,20]. However, both thermodynamics and material mixing are sensitive to the setup of numerical models, including equations of state, numerical resolution and the hydrodynamical method (Methods). To further assess the delivery of TMM to the deep mantle, we performed new MFM impact simulations with higher numerical resolution and updated equations of state[16] (Methods). The new results reproduce a similar layered structure in the post-impact Earth as in ref. 19, with the upper layer dominated by melt and vapour, and a rheologically solid lower layer (Extended Data Fig. 1 and Supplementary Video 1). The total mass of TMM within the lower layer is approximately 0.01 Earth masses, and 15% of the lower-layer TMM can be solid (Extended Data Table 2). We also performed ultra-high-resolution smoothed particle hydrodynamics (SPH) simulations of giant impacts[21] to corroborate the results (Methods). The high-resolution SPH simulations also demonstrate, as with the MFM simulations, that post-impact Earth could have retained a solid lower layer with some solid and molten TMM material (Supplementary Video 2). We found that as the numerical resolution was increased, the amount of TMM mass in Earth's lower layer and its solid fraction (up to 30%) increased considerably (Extended Data Table 3). TMM may mix with Earth's mantle at a scale smaller than our model's resolution; therefore, the size and dispersal pattern of TMM in the lower layer is not yet well constrained by our giant-impact models. Although experiments show efficient fragmentation of a body of dense fluid sinking through less dense fluid, they also show that the fragments remain tightly clustered and sink quickly at rates determined by their collective behaviour and not by their individual Stokes velocities[22]. Future laboratory experiments and higher-resolution simulations are needed to investigate the small-scale dynamics during the giant impact.

The composition of the TMM determined its intrinsic density, and thus the nature of its long-term advection in Earth's mantle. In most Moon-formation impact scenarios, the Moon is preferentially composed of Theia's mantle[3]. Given the higher FeO content of the Moon's mantle (more than 10 wt%) compared with Earth's mantle (less than 8 wt%)[23], Theia's mantle may also have been iron-rich compared to Earth's. Some of the enrichment of the Moon's FeO may have resulted from post-impact mechanisms[24], not from the high FeO content of Theia. Nevertheless, under different impact scenarios, the FeO content of Theia's mantle is estimated to be 11–40 wt%, based on Si isotopic constraints[25]. Recently, this model was extended[12] to also explain the very low $^2H/^1H$ (deuterium/hydrogen) ratio (3.91×10^{-5}) of inferred lunar interior reservoirs[26]. This model predicts that Theia's mantle contained approximately 13–18 wt% FeO (ref. 12).

Based on the results of Desch and Robinson[12], we implemented three composition models for the TMM with a fixed molar ratio of Mg/Si = 1 and a variable FeO content of 13, 15 or 17 wt% (Extended Data Table 4) to estimate the TMM density. We calculated the phase equilibria and density of TMM along Earth's geotherms using the Perple_X[27,28] code and a thermodynamic dataset[29]. We then compared the results with the densities of bulk silicate Earth (BSE)[23]. The three TMM composition models and the BSE yielded similar mineral assemblages of olivine, garnet and pyroxene under the pressure and temperature (P–T) conditions of the Earth's upper mantle, which transform into bridgmanite $(Mg,Fe,Al)(Si,Al)O_3$, magnesiowüstite (Mg,Fe)O and davemaoite $CaSiO_3$ under Earth's lower-mantle P–T conditions (Extended Data Figs. 2 and 3). We found that the TMM is approximately 2.0–3.5% denser than the BSE (Fig. 2 and Extended Data Fig. 4) throughout Earth's lower mantle.

After the impact, mantle convection is expected to develop first from the outer part of Earth's thermally stratified mantle[30], which may then have propagated downwards and mixed with the lower-mantle TMM. However, this viscous process involves a prolonged time frame during which the dense TMM in the lower layer may already have sunk deeper

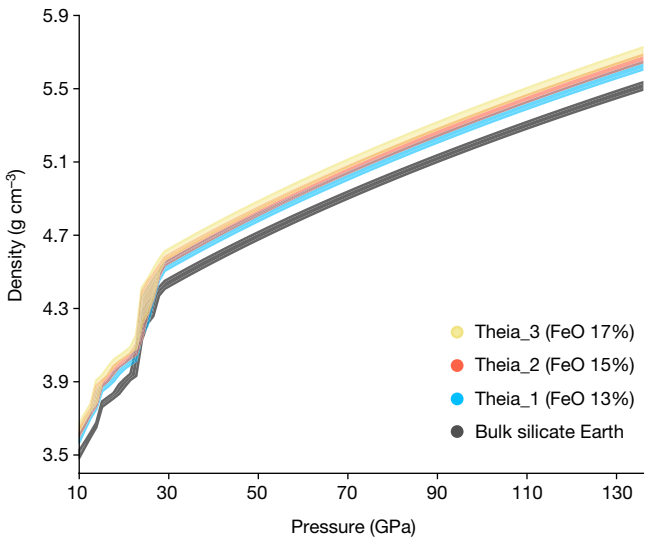

Fig. 2 | Density profiles of the TMM and the BSE as a function of pressure. The density was calculated using Perple_X[27,28] with thermodynamic data from ref. 29. The upper and lower bounds of the density profiles are, respectively, based on geotherms from Brown and Shankland[57] and Stacey[58].

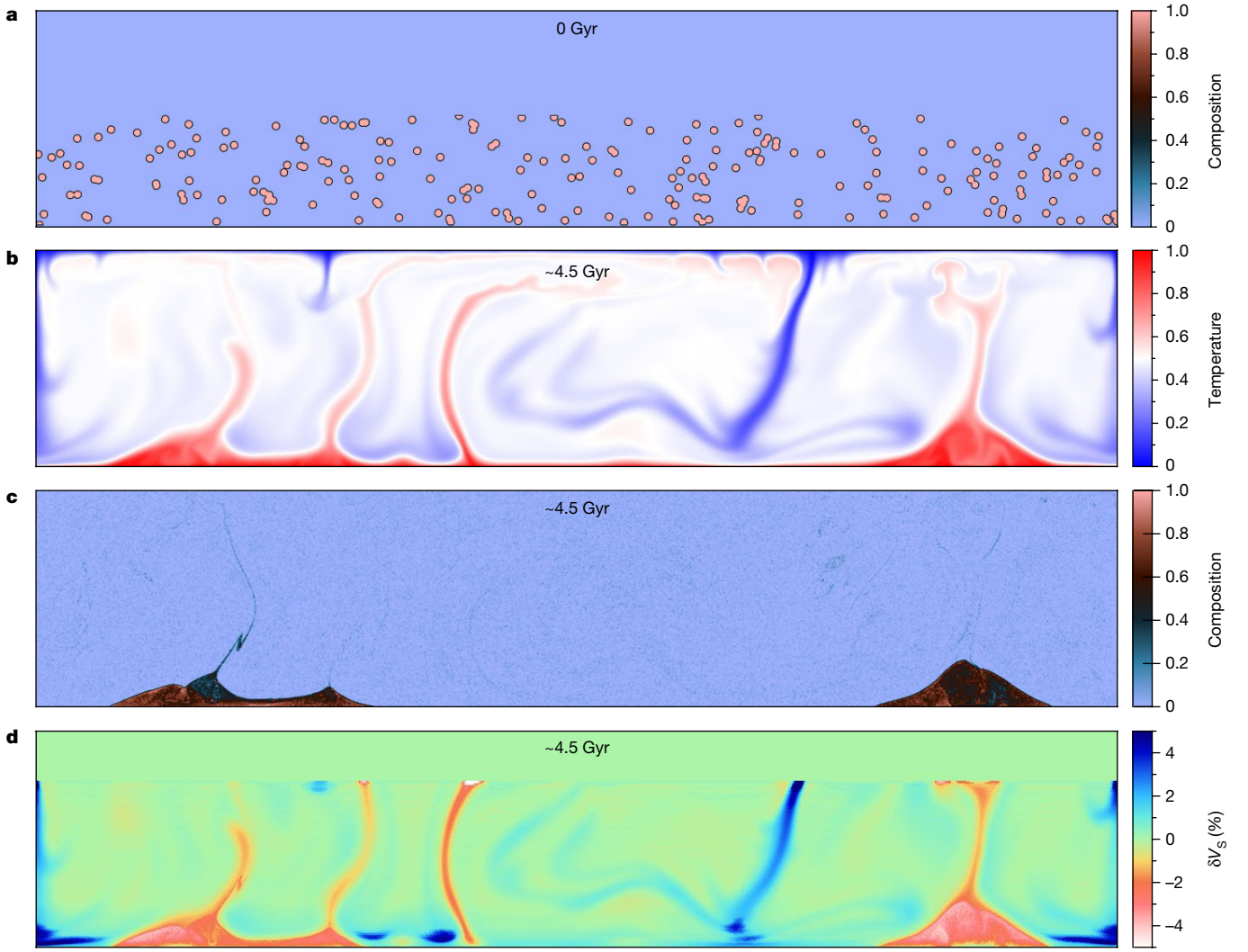

Fig. 3 | The formation of LLVP-like thermochemical piles from intrinsically dense TMM. a, Initial composition field in a geodynamic model in which the TMM is introduced into the model domain from a depth of 1,400 km to the CMB as randomly distributed spheres. **b**, Temperature field of the model at 4.5 Gyr. **c**, Composition field at 4.5 Gyr showing the formation of LLVP-like thermochemical piles due to the accumulation of TMM. The composition fields in panels **a** and **c** show pure background mantle material (0), pure TMM (1) or a mixture (intermediate values). **d**, Seismic shear velocity perturbations (δV_s) in the geodynamic model at the lower mantle depths. δV_s was calculated for each point by subtracting the average horizontal shear velocity and then dividing by this average. An adiabatic temperature gradient of 0.35 K km^{-1} was added to the temperature field to calculate the shear-wave velocity. The density and V_s were calculated using Perple_X[27,28] with the thermodynamic dataset from ref. 29.

to the CMB (Extended Data Fig. 5), thus avoiding significant stirring and mixing with materials in the upper layer. By the time it reached the CMB, the molten fraction of the TMM may also have mostly solidified due to cooling from the surroundings plus adiabatic compression. Our scaling analysis shows that a molten TMM blob would cool rapidly until it experiences a rheological transition. We estimated that the solidification timescale of a 50 km TMM blob can be as short as 1,000 years (Methods). Smaller blobs of TMM would solidify more quickly, and it is intuitive that they may sink less efficiently. However, their sinking tendency is heavily influenced by whether they are evenly dispersed within the background mantle matrix or remain clustered together[22] as well as the vigour of the convective flow in the background. To precisely determine the initial state, size, distribution and differentiation process of lower-layer TMM right before the long-term convection of Earth's solid mantle would require a combination of different equations of state for Theia and proto-Earth, unparalleled resolution for impact simulations and multiple-phase flow dynamics, which all merit future investigation. In the following, we assume a relatively short solidification timescale and treat the initially mixed molten and solid TMM in the lower mantle as all rheologically solid to explore their long-term dynamics using numerical mantle convection simulations.

Previous geodynamic modelling experiments have shown that chemical heterogeneities with an intrinsic density a few percent higher than the surrounding mantle can sink to and accumulate at the CMB[9,31–35] and that these heterogeneities can later be shaped into spatially isolated thermochemical piles that resemble the seismically observed LLVPs[36]. We designed geodynamic simulations to further investigate the advection of intrinsically dense TMM in Earth's mantle throughout Earth's history (Methods). In our reference geodynamic model, the TMM is 2.5% intrinsically denser than the surrounding mantle and is initially introduced to the lower half of the model domain as randomly distributed spheres with a fiducial radius of 50 km and a cumulative volume of approximately 4% of the two-dimensional (2D) model domain (Fig. 3a). The model starts with a uniformly hot temperature[37] to simulate the early hot mantle after the impact, but our results are not sensitive to this choice, as discussed later. After this initial state, the TMM quickly descends to the CMB and is later shaped by mantle convection into two spatially isolated thermochemical piles after 4.5 Gyr (Supplementary

Video 3). Using the temperature field and the composition field from this model (Fig. 3b,c), we calculated the seismic shear-wave velocity of the TMM piles and found that it is approximately 1–5% lower than the surrounding mantle (Fig. 3d), in agreement with the observed seismic reduction of the LLVPs[14,20,38,39]. In the model, the volume of the piles is approximately 3.4% of the mantle, which aligns with the LLVPs currently occupying a comparable volume percentage (approximately 4%) of Earth's mantle[14,20].

We additionally tested eight models with different densities (buoyancies) for the TMM (1.25%, 3.5% or 5% denser), a smaller radius for TMM blobs (25 km), radioactive heating of the TMM blobs, higher temperature dependence of the viscosity ($\times 10^5$ viscosity range owing to changes in temperature), periodic side-boundary conditions and a relatively cold initial temperature (Supplementary Videos 4–11). The physical parameters and a full list of geodynamic models are provided in Extended Data Tables 5 and 6, respectively. All of these models are characterized by similar LLVP-like piles above the CMB after 4.5 Gyr, except for one case in which the TMM was only 1.25% denser than the surrounding mantle and had a radius of 50 km and another case in which the TMM was 2.5% denser compared with the background mantle and had a small radius of 25 km. In all other cases, the higher density and larger initial size of TMM blobs increased the possibility that the TMM would sink and accumulate on the CMB and coherently persist after 4.5 Gyr.

Giant accretionary collisions can create widespread melting in the form of partial or whole silicate magma oceans[40]. Homogenization may take place during or after an impact. During solidification of the magma ocean, gravitational instability and rapid mixing can occur within the solidified region, due to convection triggered by a superadiabatic thermal profile[41,42]. Alternatively, gravitational instability can be triggered by the Fe enrichment of the upper layers during crystallization[43,44]. Recent studies have also shown that convection within the solidified mantle could become more efficient as the magma ocean crystallizes[45–47]. However, the TMMs we focus on here are incorporated into the solid lower layer, which has a lower potential temperature than the overlying molten layer. Thus, the solid and relatively cold lower layer would prohibit whole-mantle convection shortly after the impact[30], which limits mass exchange with the upper layer. Being denser than the solid background mantle, the TMM blobs considered here are likely to sink in the lower layer[48]. Similarly, the dense TMM in the upper molten layer of post-impact Earth, if it has not been completely mixed into the proto-Earth[30,49], may sink as well. A vigorously convecting magma ocean in this upper layer may lead to a large extent of mixing with the solidified mantle[50], but the effects of planetary rotation could promote the development of even large-scale mantle heterogeneities during magma ocean crystallization[51]. Thus, the approximately 0.014–0.026 $M_{\oplus}$ mass of TMM in the lower layer constrained in ref. 19 and this work is a conservative estimation of the total TMM entering the lower mantle. If the TMM remains partially molten, it may eventually accumulate at the CMB and constitute a dense basal magma ocean. A dense melt layer was assumed previously. It has been well established that it would fractionally crystallize as stable solids[2], which are later shaped by mantle convection into LLVP-like thermochemical piles.

The preservation of large-scale TMM structures in Earth's lowermost mantle has important implications for the composition and evolution of Earth's interior, the origin of the Moon and the early accretion history of the Solar System. The presence of preserved TMM piles in Earth's lower mantle implies that Earth's lowermost mantle contained large-scale heterogeneities from the beginning of Earth's evolution. The subsequent approximately 4.5 billion years of mantle convection did not erase such structures formed during Earth's primary accretionary period, consistent with evidence from the noble gases in plume-derived OIBs[11,52]. Our model, hence, suggests that constraining the composition and evolution of Earth's mantle requires consideration of heterogeneous accretions during the stage of giant impacts. Furthermore, the survival of dense basal TMM accumulations may suggest that any pre-existing ancient reservoirs (before the Moon-forming impact)[19] may also have been preserved, which could explain the observed multiple isotopic signatures that require pre-impact reservoirs[49,53].

Present-day LLVPs may be a combination of TMM and other compositional heterogeneities, for example, former subducted oceanic crust[54,55]. However, the TMM may not have fully mixed with other components, which aligns with isotopic evidence from some OIBs (having both high $^3He/^4He$ and anomalous ^{182}W) and suggests the preservation of some ancient, deep-mantle, primordial reservoirs that were least modified by recycled crust[56]. Although some of these signatures may be attributed to core–mantle interactions in the Earth[56,57], the fact that similar signatures of primordial noble gases are found in KREEP-bearing mare basalts[15] suggests the signatures in both bodies may derive from TMM. Further studies about the chemical and isotopic compositions of LLVP-related plume samples, and comparisons to lunar mare basalts may be used to further test the hypothesis. Finally, given how common giant impacts were during the late stages of planetary accretion[58], compositional heterogeneities from large impactors may be preserved in other solid planets as well.

Online content

Any methods, additional references, Nature Portfolio reporting summaries, source data, extended data, supplementary information, acknowledgements, peer review information; details of author contributions and competing interests; and statements of data and code availability are available at https://doi.org/10.1038/s41586-023-06589-1.

1. Garnero, E. J., McNamara, A. K. & Shim, S. H. Continent-sized anomalous zones with low seismic velocity at the base of Earth's mantle. *Nat. Geosci.* **9**, 481–489 (2016).
2. Labrosse, S., Hernlund, J. W. & Coltice, N. A crystallizing dense magma ocean at the base of the Earth's mantle. *Nature* **450**, 866–869 (2007).
3. Canup, R. M. & Asphaug, E. Origin of the Moon in a giant impact near the end of the Earth's formation. *Nature* **412**, 708–712 (2001).
4. Kokubo, E. & Ida, S. Orbital evolution of protoplanets embedded in a swarm of planetesimals. *Icarus* **114**, 247–257 (1995).
5. Cameron, A. G. W. & Ward, W. R. The origin of the Moon. *Abstr. Lunar Planet. Sci. Conf.* **7**, 120–122 (1976).
6. Ringwood, A. E. Volatile and siderophile element geochemistry of the Moon: a reappraisal. *Earth Planet. Sci. Lett.* **111**, 537–555 (1992).
7. Nie, N. X. & Dauphas, N. Vapor drainage in the protolunar disk as the cause for the depletion in volatile elements of the Moon. *Astrophys. J.* **884**, L48 (2019).
8. Lee, C. T. A. et al. Upside-down differentiation and generation of a primordial lower mantle. *Nature* **463**, 930–933 (2010).
9. Christensen, U. R. & Hofmann, A. W. Segregation of subducted oceanic crust in the convecting mantle. *J. Geophys. Res.* **99**, 19867–19884 (1994).
10. Williams, C. D., Mukhopadhyay, S., Rudolph, M. L. & Romanowicz, B. Primitive helium is sourced from seismically slow regions in the lowermost mantle. *Geochem. Geophys. Geosyst.* **20**, 4130–4145 (2019).
11. Mukhopadhyay, S. Early differentiation and volatile accretion recorded in deep-mantle neon and xenon. *Nature* **486**, 101–104 (2012).
12. Desch, S. J. & Robinson, K. L. A unified model for hydrogen in the Earth and Moon: no one expects the Theia contribution. *Chemie der Erde* **79**, 125546 (2019).
13. Pepin, R. O. & Porcelli, D. Origin of noble gases in the terrestrial planets. *Rev. Mineral. Geochem.* **47**, 191–246 (2002).
14. Burke, K., Steinberger, B., Torsvik, T. H. & Smethurst, M. A. Plume generation zones at the margins of large low shear velocity provinces on the core–mantle boundary. *Earth Planet. Sci. Lett.* **265**, 49–60 (2008).
15. Will, P., Busemann, H., Riebe, M. E. I. & Maden, C. Indigenous noble gases in the Moon's interior. *Sci. Adv.* **8**, 1–9 (2022).
16. Stewart, S. et al. The shock physics of giant impacts: key requirements for the equations of state. *AIP Conf. Proc.* **2272**, 080003 (2020).
17. Kegerreis, J. A., Eke, V. R., Massey, R. J., Sandnes, T. D. & Teodoro, L. F. A. Immediate origin of the Moon as a post-impact satellite. *Astrophys. J. Lett.* **937**, L40 (2022).
18. Deng, H. et al. Enhanced mixing in Giant Impact simulations with a new Lagrangian method. *Astrophys. J.* **870**, 127 (2019).
19. Deng, H. et al. Primordial Earth mantle heterogeneity caused by the Moon-forming Giant Impact? *Astrophys. J.* **887**, 211 (2019).
20. Cottaar, S. & Lekic, V. Morphology of seismically slow lower-mantle structures. *Geophys. J. Int.* **207**, 1122–1136 (2016).
21. Kegerreis, J. A. et al. Planetary giant impacts: convergence of high-resolution simulations using efficient spherical initial conditions and SWIFT. *Mon. Not. R. Astron. Soc.* **487**, 5029–5040 (2019).
22. Deguen, R., Landeau, M. & Olson, P. Turbulent metal–silicate mixing, fragmentation, and equilibration in magma oceans. *Earth Planet. Sci. Lett.* **391**, 274–287 (2014).

23. Dauphas, N., Burkhardt, C., Warren, P. H. & Fang-Zhen, T. Geochemical arguments for an Earth-like Moon-forming impactor. *Philos. Trans. R. Soc. A* **372**, 20130244 (2014).
24. Pahlevan, K., Stevenson, D. J. & Eiler, J. M. Chemical fractionation in the silicate vapor atmosphere of the Earth. *Earth Planet. Sci. Lett.* **301**, 433–443 (2011).
25. Meier, M. M. M., Reufer, A. & Wieler, R. On the origin and composition of Theia: constraints from new models of the Giant Impact. *Icarus* **242**, 316–328 (2014).
26. Robinson, K. L. et al. Water in evolved lunar rocks: evidence for multiple reservoirs. *Geochim. Cosmochim. Acta* **188**, 244–260 (2016).
27. Connolly, J. A. D. Computation of phase equilibria by linear programming: a tool for geodynamic modeling and its application to subduction zone decarbonation. *Earth Planet. Sci. Lett.* **236**, 524–541 (2005).
28. Connolly, J. A. D. The geodynamic equation of state: what and how. *Geochem. Geophys. Geosyst.* **10**, 1–19 (2009).
29. Stixrude, L. & Lithgow-Bertelloni, C. Thermodynamics of mantle minerals – II. Phase equilibria. *Geophys. J. Int.* **184**, 1180–1213 (2011).
30. Nakajima, M. & Stevenson, D. J. Melting and mixing states of the Earth's mantle after the Moon-forming impact. *Earth Planet. Sci. Lett.* **427**, 286–295 (2015).
31. Gurnis, M. The effects of chemical density differences on convective mixing in the Earth's mantle. *J. Geophys. Res., Solid Earth* **91**, 11407–11419 (1986).
32. Tackley, P. J. in *The Core-Mantle Boundary Region* (eds Gurnis, M., Wysession, M. E., Knittle, E. & Buffet, B. A.) 231–253 (American Geophysical Union, 1998).
33. Nakagawa, T., Tackley, P. J., Deschamps, F. & Connolly, J. A. D. The influence of MORB and harzburgite composition on thermo-chemical mantle convection in a 3-D spherical shell with self-consistently calculated mineral physics. *Earth Planet. Sci. Lett.* **296**, 403–412 (2010).
34. Gu, T., Li, M., McCammon, C. & Lee, K. K. M. Redox-induced lower mantle density contrast and effect on mantle structure and primitive oxygen. *Nat. Geosci.* **9**, 723–727 (2016).
35. Yuan, Q. & Li, M. Instability of the African large low-shear-wave-velocity province due to its low intrinsic density. *Nat. Geosci.* **15**, 334–339 (2022).
36. McNamara, A. K. & Zhong, S. Thermochemical structures beneath Africa and the Pacific Ocean. *Nature* **437**, 1136–1139 (2005).
37. O'Neill, C., Marchi, S., Zhang, S. & Bottke, W. Impact-driven subduction on the Hadean Earth. *Nat. Geosci.* **10**, 793–797 (2017).
38. Hernlund, J. W. & Houser, C. On the statistical distribution of seismic velocities in Earth's deep mantle. *Earth Planet. Sci. Lett.* **265**, 423–437 (2008).
39. Lei, W. et al. Global adjoint tomography – model GLAD-M25. *Geophys. J. Int.* **223**, 1–21 (2020).
40. Elkins-Tanton, L. T. Magma oceans in the inner Solar System. *Annu. Rev. Earth Planet. Sci.* **40**, 113–139 (2012).
41. Abe, Y. Thermal and chemical evolution of the terrestrial magma ocean. *Phys. Earth Planet. Inter.* **1**, 27–39 (1997).
42. Solomatov, V. S. in *Treatise on Geophysics* 1st edn, Vol. 9 (ed. Schubert, G.) 91–119 (Elsevier, 2007).
43. Maurice, M. et al. Onset of solid-state mantle convection and mixing during magma ocean solidification. *J. Geophys. Res., Planets* **122**, 577–598 (2017).
44. Boukaré, C. E., Parmentier, E. M. & Parman, S. W. Timing of mantle overturn during magma ocean solidification. *Earth Planet. Sci. Lett.* **491**, 216–225 (2018).
45. Labrosse, S., Morison, A., Deguen, R. & Alboussière, T. Rayleigh–Bénard convection in a creeping solid with melting and freezing at either or both its horizontal boundaries. *J. Fluid Mech.* **846**, 5–36 (2018).
46. Agrusta, R. et al. Mantle convection interacting with magma oceans. *Geophys. J. Int.* **220**, 1878–1892 (2020).
47. Morison, A., Labrosse, S., Deguen, R. & Alboussière, T. Timescale of overturn in a magma ocean cumulate. *Earth Planet. Sci. Lett.* **516**, 25–36 (2019).
48. Becker, T. W., Kellogg, J. B. & O'Connell, R. J. Thermal constraints on the survival of primitive blobs in the lower mantle. *Earth Planet. Sci. Lett.* **171**, 351–365 (1999).
49. Lock, S. J., Bermingham, K. R., Parai, R. & Boyet, M. Geochemical constraints on the origin of the Moon and preservation of ancient terrestrial heterogeneities. *Space Sci. Rev.* **216**, 1–46 (2020).
50. Ballmer, M. D., Lourenço, D. L., Hirose, K., Caracas, R. & Nomura, R. Reconciling magma-ocean crystallization models with the present-day structure of the Earth's mantle. *Geochem. Geophys. Geosyst.* **18**, 2785–2806 (2017).
51. Maas, C. & Hansen, U. Dynamics of a terrestrial magma ocean under planetary rotation: a study in spherical geometry. *Earth Planet. Sci. Lett.* **513**, 81–94 (2019).
52. Williams, C. D. & Mukhopadhyay, S. Capture of nebular gases during Earth's accretion is preserved in deep-mantle neon. *Nature* **565**, 78–81 (2019).
53. Mundl-Petermeier, A. et al. Temporal evolution of primordial tungsten-182 and $^{3}He/^{4}He$ signatures in the Iceland mantle plume. *Chem. Geol.* **525**, 245–259 (2019).
54. Li, M., McNamara, A. K. & Garnero, E. J. Chemical complexity of hotspots caused by cycling oceanic crust through mantle reservoirs. *Nat. Geosci.* **7**, 366–370 (2014).
55. Mulyukova, E., Steinberger, B., Dabrowski, M. & Sobolev, S. V. Survival of LLSVPs for billions of years in a vigorously convecting mantle: replenishment and destruction of chemical anomaly. *J. Geophys. Res., Solid Earth* **120**, 3824–3847 (2015).
56. Jackson, M. G. et al. Ancient helium and tungsten isotopic signatures preserved in mantle domains least modified by crustal recycling. *Proc. Natl Acad. Sci. USA* **117**, 30993–31001 (2020).
57. Brown, J. M. & Shankland, T. J. Thermodynamic parameters in the Earth as determined from seismic profiles. *Geophys. J. R. Astron. Soc.* **66**, 579–596 (1981).
58. Stacey, F. D. A thermal model of the earth. *Phys. Earth Planet. Inter.* **15**, 341–348 (1977).

Methods

Giant-impact simulations

Simulations of the giant impact are subject to uncertainties arising from the hydrodynamic methods[18,59,60], the treatment of contact discontinuities and free surfaces[61,62], the equations of state[16,63] and the numerical resolution[21,64,65]. The SPH method is widely used in giant-impact simulations[3]. However, standard SPH schemes and common forms of artificial viscosity, which are used to maintain differentiability across shocks in SPH, allow for the triggering of numerical viscosity that can suppress turbulence and mixing[18,66] and cause overheating[67]. Methodological developments to limit the application of artificial viscosity are ongoing, including revisions to the SPH equations[68], developing new forms of artificial viscosity (for example, ref. 69) or using methods without artificial viscosity altogether[18]. Simply increasing the resolution also reduces its fractional effect on the whole simulation. Here we analyse models from ultra-high-resolution SPH simulations[17] and a new meshless method[18]. Despite the differences in the hydrodynamic methods, equations of state and resolution, we derived qualitatively similar results, namely, a solid lower mantle in the proto-Earth after a canonical impact with approximately 0.01 $M_\oplus$ of Theia material implanted into it.

Giant-impact models with SPH simulations

The SPH simulations were run using the open-source hydrodynamics and gravity code SWIFT[70], using 10^8 SPH particles (and lower-resolution comparisons). The initial conditions and full details are provided in ref. 17. The initial conditions were created using the publicly available WoMa and SEAGen packages[21,71]. Our numerical resolution is considerably greater than the 10^5–10^6 particle resolution often used in standard Moon-formation studies, which enables the detailed study of the relatively small mass of TMM implanted into the deep Earth mantle.

To model the core and mantle materials, we use the updated ANEOS $Fe_{85}Si_{15}$ and forsterite equations of state[16]. These allow direct examination of the phase state of TMM and other material, in addition to checking the overall change in entropy. The physical parameters for the impact simulations are the same as in ref. 17.

The simulations involve collisions between a low-mass (approximately 0.1 $M_\oplus$) Theia and a large proto-Earth (0.9 $M_\oplus$), at impact angles of 45° and impact speeds at contact near the mutual escape speed, but with seven different model resolutions (Extended Data Table 3). All simulations produced a similar layered structure for the post-impact Earth with a mostly solid lower mantle. However, the mass and solid fraction of TMM implanted into the lower layer are not adequately resolved for numbers of particles below 10^7. Even with 10^8 particles, the precise values have not fully converged, although the overall behaviour is consistent.

Although the simulations conducted in this study used low impactor masses of approximately 0.1 $M_\oplus$, we anticipate that the preservation of TMM in Earth's deep mantle may be also possible if Theia has a larger mass, as more TMM is likely to be implanted at greater initial depths and the FeO content (and thus density) of TMM could be higher[25]. Therefore, the Theia origin for the LLVPs that we consider here may be not restricted to the canonical-like impact scenarios, but the post-impact composition, thermal state of the lower mantle and mantle mixing in a wider range of impact conditions[12,72] would need to be investigated in detail, including with robust numerical treatments, to directly assess this claim.

Giant-impact models in MFM simulations

The MFM simulations were carried out with the open-source code GIZMO[73]. The method captures shocks with a Riemann solver and is, thus, free of artificial viscosity. MFM captures subsonic turbulence better than traditional SPH at a comparable resolution[73] and, thus, mixing in giant-impact simulations[18]. The MFM simulations cover a larger parameter space than the expensive ultra-high-resolution SPH simulations. The simulations described in ref. 19 used the ANEOS/M-ANEOS[74,75] equations of state with iron comprising the core and forsterite comprising the mantle. It employed 5×10^5 particles. To explore the robustness of our results with respect to the equations of states and resolution, we then adopted the latest equations of state from ref. 16 and ran new simulations, as listed in Extended Data Table 2, with 2×10^6 or 10×10^6 particles.

Thanks to the new equations of state with explicit phase information, we can identify the rheological transition in the mantle material (Extended Data Fig. 1). The radius of this rheological transition lies slightly beneath the entropy jump reported in ref. 19. Such entropy jumps are due to focused shock heating and concurrent supersonic flows in the upper mantle and are coincident with a compositional change[19]. More than 0.01 $M_\oplus$ of TMM is consistently found in the lower Earth mantle, which is largely solid.

Thermal evolution model of Theia mantle blobs

We modelled the thermal evolution of the approximately 90% of the TMM blobs in the lower layer that were non-solid. These non-solid TMM blobs have a potential temperature of 5,000–8,000 K after the impact. The results of high-pressure melting experiments suggest that such blobs are entirely molten, even in the deep mantle[76,77]. They are, thus, likely to be cooled by thermal convection until the melt fraction becomes low enough to experience the rheological transition[42,78]. We estimated the cooling timescale using a scaling analysis of convective heat flux. The heat flux out of the upper hemisphere F_c [W] is roughly given by

$$F_c \approx \pi r_{TMM}^2 \times k_T \frac{T_{TMM} - T_m}{r_{TMM}} \left(\frac{Ra}{Ra_c} \right)^{1/3},$$

where k_T is the thermal conductivity, r_{TMM} and T_{TMM} are the radius and temperature of Theia mantle blobs, T_m is the temperature of the surrounding mantle, Ra is the internal Rayleigh number and Ra_c (approximately 1,000) is the critical Rayleigh number. Assuming a melt viscosity of $\eta = 100$ Pa s and a heat capacity of 1,000 J kg^{-1} K^{-1}, the cooling timescale is predicted to be shorter than 1,000 years for a 50-km-sized blob, regardless of the initial temperature. During this period, the TMM melt may also migrate through the surrounding mantle by melt percolation. However, according to the giant-impact models, the temperature of the deep lower mantle is below the solidus, and thus, a channelized melt flow would likely freeze soon after leaving the TMM blobs. Furthermore, even if the TMM melt were able to raise the temperature of the surrounding mantle to melt it, the porosity expected would be minimal, and therefore, percolation through such a mostly solidified mantle would be negligible. Additionally, given that the TMM blobs are embedded in the ductile lower mantle, crack formation via fracturing is not an effective mechanism for melt migration.

The subsequent evolution of rheologically solid TMM would again be governed by percolation, which separates the melt and liquid phases within the blob. Depending on the density contrast between the melt and solid, the melt may migrate either upwards or downwards[79–81], creating some degree of fractionation. Regardless of the direction, however, the melt would be expected to solidify as it reaches the rim of the Theia mantle blobs. The melt would also solidify by adiabatic compression as the blobs sink through the ambient mantle. Considering the estimated short percolation timescale in comparison to the long timescale of the viscous flow, it is plausible that the blobs would solidify before they reach the CMB.

Setup of the mantle convection model

Here, we provide the governing equations that are used to solve the mantle convection models in our modified 2D Citcom code. Complete

descriptions are available from ref. 82 and references therein. We performed the geodynamic calculations by solving the following non-dimensional equations for conservation of mass, momentum and energy under the Boussinesq approximation:

$$\nabla \cdot \mathbf{u} = 0 \tag{1}$$

$$-\nabla P + \nabla \cdot (\eta \epsilon) = \mathrm{Ra}(T - BC)\mathbf{z} \tag{2}$$

$$\frac{\partial T}{\partial t} + (\mathbf{u} \cdot \nabla) T = \nabla^2 T + Q \tag{3}$$

where $\mathbf{u}$ is the velocity, P is the dynamic pressure, η is the viscosity, ϵ is the strain rate, Ra is the Rayleigh number, T is the temperature, and B and C are the buoyancy number and composition, respectively. $\mathbf{z}$ is the unit vector in the vertical direction, t is time and Q is the internal heating rate. α and κ are the thermal expansivity and thermal diffusivity, respectively.

The advection of the composition C is given by:

$$\frac{\partial C}{\partial t} + (\mathbf{u} \cdot \nabla) C = 0 \tag{4}$$

The viscosity is defined as:

$$\eta = \eta_r \eta_c \exp[A(0.5 - T)] \tag{5}$$

where A is the activation coefficient for the temperature dependence of the viscosity. η_c is a parameter that determines the intrinsic viscosity. The viscosity prefactor η_r is 1.0 in the upper mantle and 50.0 in the lower mantle, resulting in a ×50 viscosity increase across the 660 km discontinuity. We used an activation coefficient of $A = 9.21$ in most cases, but a value of $A = 11.51$ was also explored to test an even higher temperature-dependent viscosity range owing to changes in temperature.

The simulation was computed in a 2D Cartesian geometry with an aspect ratio of 5:1. To solve the conservation equations, we used a modified version of the convection code Citcom[82], which includes thermochemical convection and both composition- and temperature-dependent rheology. As is appropriate for 2D Cartesian models[83], we excluded internal heating in most calculations, but models with radioactive heating of the TMM were also tested. The initial temperature was 0.72 (non-dimensional) everywhere with small perturbations, and we also tested a model with a different initial temperature. The top and bottom surfaces were isothermal with $T = 0$ and $T = 1$, respectively. All boundaries were free-slip. The side boundaries were reflective and insulating, but we also tested a model with periodic side boundaries. The compositional field was advected using approximately 7.9 million tracers with the ratio-tracer method[84]. The diffusion time was dimensionalized using $t = (h^2/\kappa)t'$, where t is dimensional time, t' is non-dimensional time, h is the thickness of the mantle (here, $h = 2{,}890$ km) and κ is the thermal diffusivity (here, $\kappa = 1 \times 10^{-6}\ \mathrm{m^2\ s^{-1}}$).

Data availability

All data and parameters are available in the main text or the supplementary materials. The data that support the findings of this study are also available at https://doi.org/10.6084/m9.figshare.24013776.v1. Source data are provided with this paper.

Code availability

The author's modified 2D Citcom code used in this study is available from https://figshare.com/projects/Yuan_Li_2022_NG/129185. The GIZMO code is made available at http://www.tapir.caltech.edu/~phopkins/Site/GIZMO.html. SWIFT is publicly available at http://swiftsim.com. WoMa is publicly available at https://github.com/srbonilla/WoMa, or the Python module can be installed directly with pip (https://pypi.org/project/woma/).

59. Canup, R. M., Barr, A. C. & Crawford, D. A. Lunar-forming impacts: high-resolution SPH and AMR-CTH simulations. *Icarus* **222**, 200–219 (2013).
60. Hosono, N., Saitoh, T. R., Makino, J., Genda, H. & Ida, S. The Giant Impact simulations with density independent smoothed particle hydrodynamics. *Icarus* **271**, 131–157 (2016).
61. Reinhardt, C. & Stadel, J. Numerical aspects of Giant Impact simulations. *Mon. Not. R. Astron. Soc.* **467**, 4252–4263 (2017).
62. Ruiz-Bonilla, S. et al. Dealing with density discontinuities in planetary SPH simulations. *Mon. Not. R. Astron. Soc.* **512**, 4660–4668 (2022).
63. Hosono, N. & Karato, S. The influence of equation of state on the Giant Impact simulations. *J. Geophys. Res., Planets* **127**, 1–18 (2022).
64. Hosono, N. et al. Unconvergence of very-large-scale Giant Impact simulations. *Publ. Astron. Soc. Jpn* **69**, 1–11 (2017).
65. Meier, T., Reinhardt, C. & Stadel, J. G. The EOS/resolution conspiracy: convergence in proto-planetary collision simulations. *Mon. Not. R. Astron. Soc.* **1816**, 1806–1816 (2021).
66. Raskin, C. & Owen, J. M. Examining the accuracy of astrophysical disk simulations with a generalized hydrodynamical test problem. *Astrophys. J.* **831**, 26 (2016).
67. Gabriel, T. S. J. & Allen-Sutter, H. Dependencies of mantle shock heating in pairwise accretion. *Astrophys. J. Lett.* **915**, L32 (2021).
68. Frontiere, N., Raskin, C. D. & Owen, J. M. CRKSPH – a conservative reproducing kernel smoothed particle hydrodynamics scheme. *J. Comput. Phys.* **332**, 160–209 (2017).
69. Rosswog, S. Astrophysical smooth particle hydrodynamics. *New Astron. Rev.* **53**, 78–104 (2009).
70. Schaller, M. et al. SWIFT: SPH with inter-dependent fine-grained tasking. In *Astrophysics Source Code Library*, ascl-1805 (2018).
71. Ruiz-Bonilla, S., Eke, V. R., Kegerreis, J. A., Massey, R. J. &Teodoro, L. F. A. The effect of pre-impact spin on the Moon-forming collision. *Mon. Not. R. Astron. Soc.* **2870**, 2861–2870 (2021).
72. Canup, R. M. Forming a Moon with an Earth-like composition via a giant impact. *Science* **338**, 1052–1056 (2012).
73. Hopkins, P. F. A new class of accurate, mesh-free hydrodynamic simulation methods. *Mon. Not. R. Astron. Soc.* **450**, 53–110 (2015).
74. Thompson, S. L. & Lauson, H. S. *Improvements in the Chart D Radiation—Hydrodynamic Code. III. Revised Analytic Equation of State.* Sandia Report SC-RR-71 0174 (1972).
75. Melosh, H. J. A hydrocode equation of state for SiO_2. *Meteorit. Planet. Sci.* **42**, 2079–2098 (2007).
76. Fiquet, G. et al. Melting of peridotite to 140 gigapascals. *Science* **329**, 1516–1518 (2010).
77. Andrault, D. et al. Solidus and liquidus profiles of chondritic mantle: implication for melting of the Earth across its history. *Earth Planet. Sci. Lett.* **304**, 251–259 (2011).
78. Abe, Y. in *Evolution of the Earth and Planets* (eds Takahashi, E., Jeanloz, R. & Rubie, D.) 41–54 (American Geophysical Union, 1993).
79. Miyazaki, Y. & Korenaga, J. On the timescale of magma ocean solidification and its chemical consequences: 2. Compositional differentiation under crystal accumulation and matrix compaction. *J. Geophys. Res., Solid Earth* **124**, 3399–3419 (2019).
80. Nomura, R. et al. Spin crossover and iron-rich silicate melt in the Earth's deep mantle. *Nature* **473**, 199–202 (2011).
81. Andrault, D. et al. Solid–liquid iron partitioning in Earth's deep mantle. *Nature* **487**, 354–357 (2012).
82. Moresi, L. N. & Solomatov, V. S. Numerical investigation of 2D convection with extremely large viscosity variations. *Phys. Fluids* **7**, 2154–2162 (1995).
83. Farrell, K. A. O. & Lowman, J. P. Emulating the thermal structure of spherical shell convection in plane-layer geometry mantle convection models. *Phys. Earth Planet. Inter.* **182**, 73–84 (2010).
84. Tackley, P. J. & King, S. D. Testing the tracer ratio method for modeling active compositional fields in mantle convection simulations. *Geochem. Geophys. Geosyst.* **4**, 1–15 (2003).
85. Schaller, M. et al. Swift: a modern highly-parallel gravity and smoothed particle hydrodynamics solver for astrophysical and cosmological applications. Preprint at http://arxiv.org/abs/2305.13380 (2023).
86. Hirth, G. & Kohlstedt, D. L. Water in the oceanic upper mantle: implications for rheology, melt extraction and the evolution of the lithosphere. *Earth Planet. Sci. Lett.* **144**, 93–108 (1996).
87. Dziewonski, A. M. & Anderson, D. L. Preliminary reference Earth model. *Phys. Earth Planet. Inter.* **25**, 297–356 (1981).

Acknowledgements We thank M. Gurnis, D. Stevenson, R. Canup, P. Olson, S. Stewart, M. Zolotov, T. Becker, M. Jackson, S.-H. Shim, D. Grady, R. Shi and S. Yuan for their support, discussions and insights. The numerical models were performed on the Agave cluster at Arizona State University. Any use of trade, firm or product names is for descriptive purposes only and does not imply endorsement by the U.S. Government. This work is supported by National Science Foundation grants EAR-1849949, EAR-1855624 and EAR-2216564. Q.Y. acknowledges support from the O. K. Earl Postdoctoral Fellowship at Caltech. T.S.J.G. recognizes support from the U.S. Geological Survey, Astrogeology Science Center. J.A.K. acknowledges support from a NASA Postdoctoral Program Fellowship, administered by Oak Ridge Associated Universities. Y.M. acknowledges a Stanback Postdoctoral Fellowship from the Caltech Center for Comparative Planetary Evolution. V.R.E. is supported by Science and Technology Facilities Council (STFC) grant ST/T000244/1. The MFM giant-impact simulations were performed on the Piz Daint supercomputer of the Swiss Nation Supercomputing Centre and the local cluster of the Shanghai Astronomical Observatory. The research in this paper made use of the SWIFT

open-source simulation code[70,85], v.0.9.0. This work used the DiRAC@Durham facility managed by the Institute for Computational Cosmology on behalf of the STFC DiRAC High-Performance Computing Facility (www.dirac.ac.uk). The equipment was funded by capital funding from the Department for Business, Energy and Industrial Strategy via STFC capital grants ST/K00042X/1, ST/P002293/1, ST/R002371/1 and ST/S002502/1, Durham University and STFC operations grant ST/R000832/1. DiRAC is part of the National e-Infrastructure.

Author contributions Q.Y. and E.J.G. conceptualized the initial idea. Q.Y., M.M.L. and E.J.G. designed the study. Q.Y. performed and analysed the geodynamic models with supervision from M.M.L. S.J.D. constrained the impact scenario and provided the composition of Theia. B.K. and Q.Y. computed the thermodynamic and seismic calculations. H.P.D., J.A.K. and V.R.E. performed the impact simulations and analysed the results. T.S.J.G. performed independent verifications of the SPH results and consulted on the SPH numerics. Y.M. developed the thermal evolution model. P.D.A. examined the fragmentation, dilution effect and magma mixing associated with the impact. All authors contributed to the writing and editing of the manuscript.

Competing interests The authors declare no competing interests.

Additional information

Supplementary information The online version contains supplementary material available at https://doi.org/10.1038/s41586-023-06589-1.

Correspondence and requests for materials should be addressed to Qian Yuan.

Peer review information *Nature* thanks Stéphane Labrosse and the other, anonymous, reviewer(s) for their contribution to the peer review of this work.

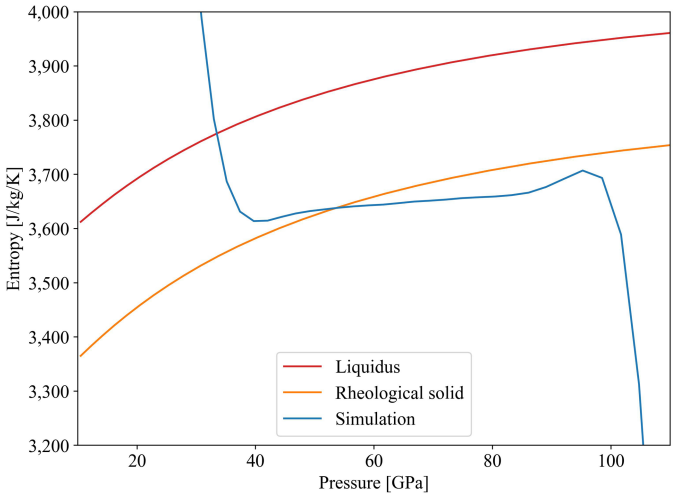

Extended Data Fig. 1 | Entropy profile (blue, in $Jkg^{-1}K^{-1}$) of mantle material in the post-impact Earth for our impact model using the meshless finite mass (MFM) method[18]. The red curve shows the liquidus of forsterite[16] and the rheological transition of the mantle was marked by the orange curve where the melt fraction above that depth becomes larger than 40%[42,86].

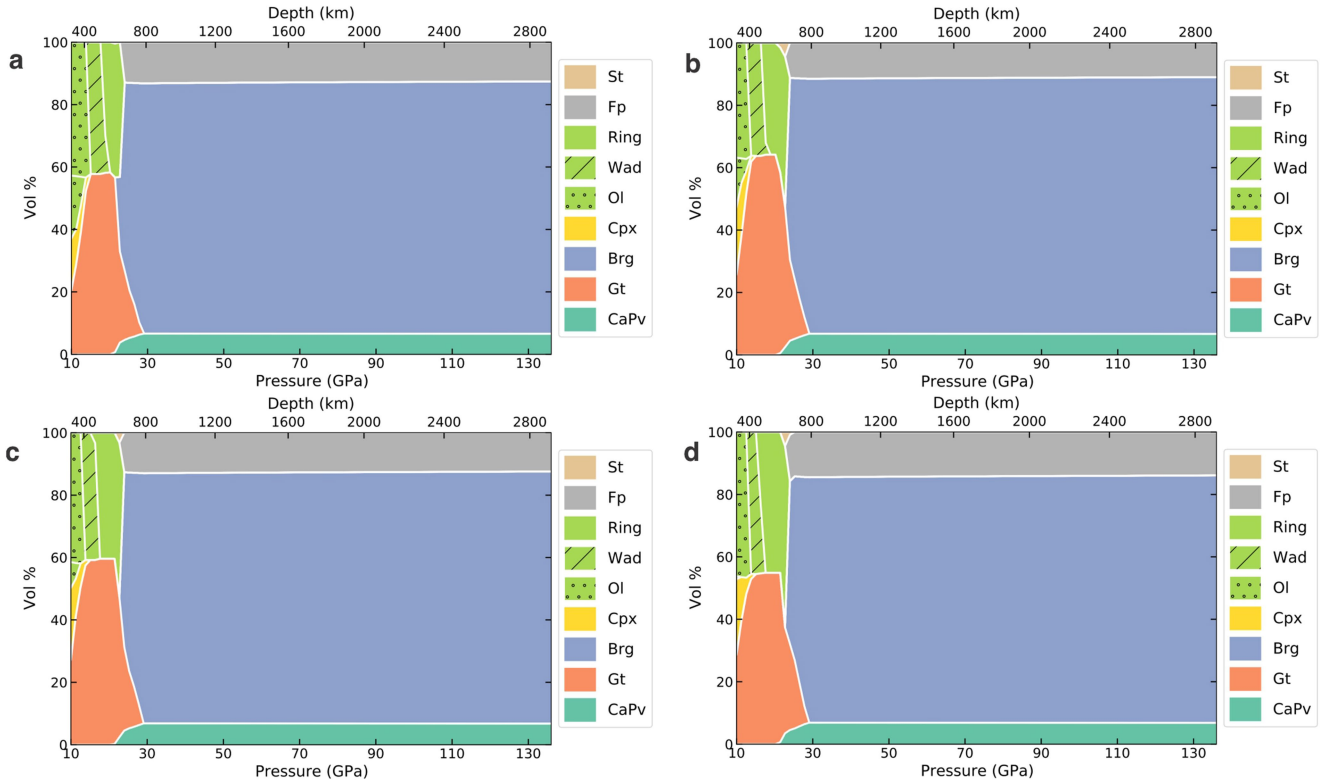

Extended Data Fig. 2 | Phase diagrams of the bulk silicate Earth (a), Theia_1 (b), Theia_2 (c) and Theia_3 (d) with geotherm from ref. 57. The FeO contents of Theia are 13 wt% (Theia_1), 15 wt% (Theia_2), and 17 wt% (Theia_3), respectively. Phase equilibria were calculated using Perple_X[27,28] with thermodynamic data from ref. 29. St: stishovite, Fp: ferropericlase, Ring: ringwoodite, Wad: wadsleyite, Ol: olivine, Cpx: clinopyroxene, Brg: bridgmanite, Gt: garnet, CaPv: davemaoite.

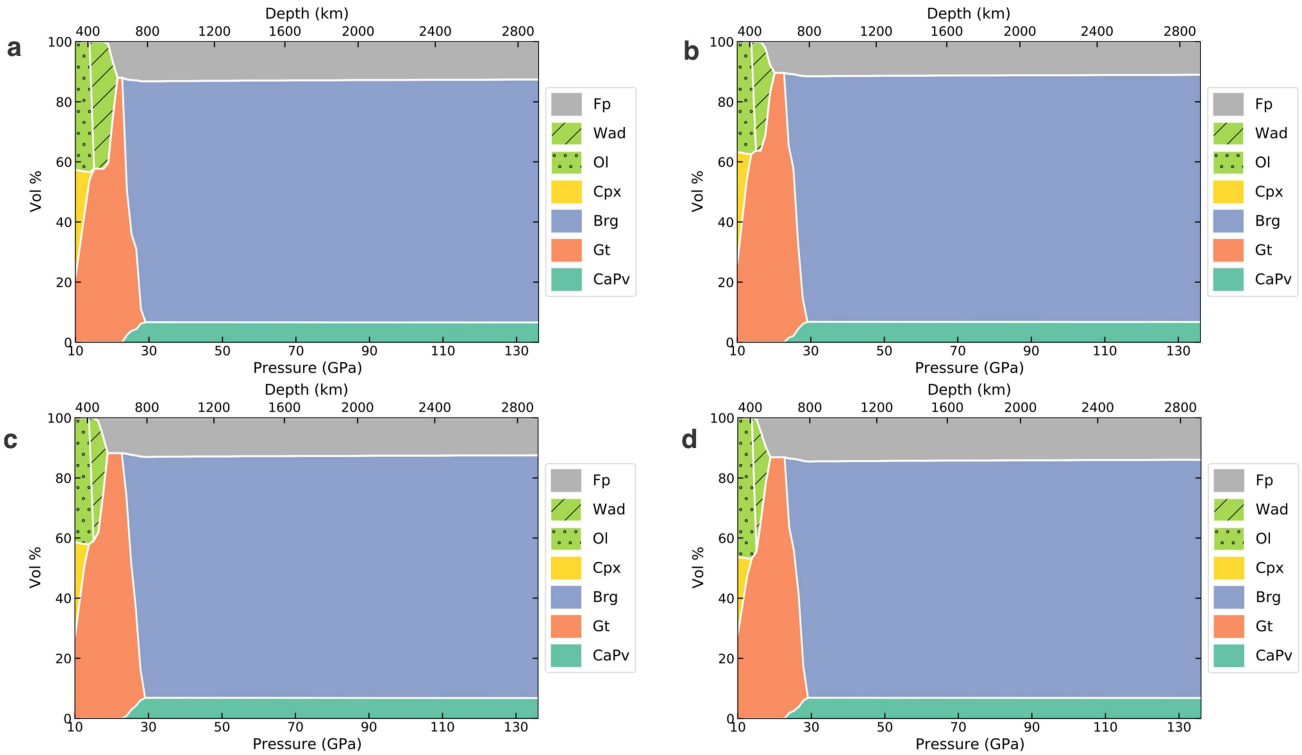

Extended Data Fig. 3 | Phase diagrams of the bulk silicate Earth (a), Theia_1 (b), Theia_2 (c) and Theia_3 (d) with geotherm from ref. 58. The FeO contents of Theia are 13 wt% (Theia_1), 15 wt% (Theia_2), and 17 wt% (Theia_3), respectively. Phase equilibria were calculated using Perple_X[27,28] with thermodynamic data from ref. 29. Fp: ferropericlase, Wad: wadsleyite, Ol: olivine, Cpx: clinopyroxene, Brg: bridgmanite, Gt: garnet, CaPv: davemaoite.

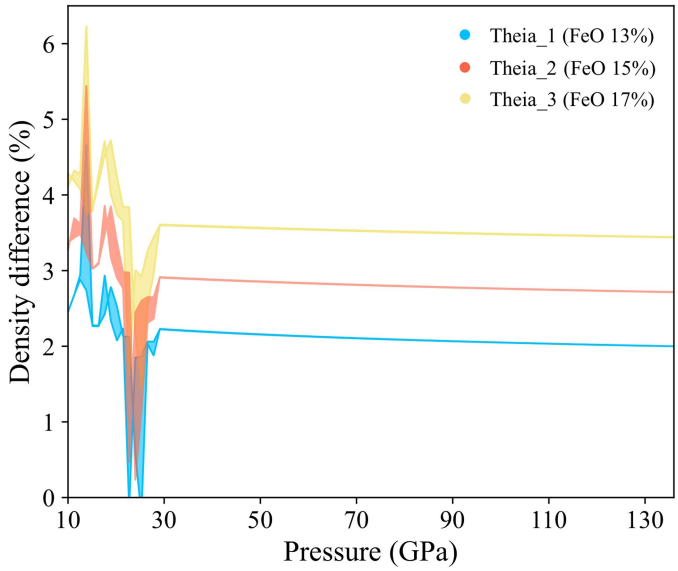

Extended Data Fig. 4 | Density difference between Theia mantle material and the bulk silicate Earth as a function of pressure. Phase equilibria were calculated using Perple_X[27,28] with thermodynamic data from ref. 29.

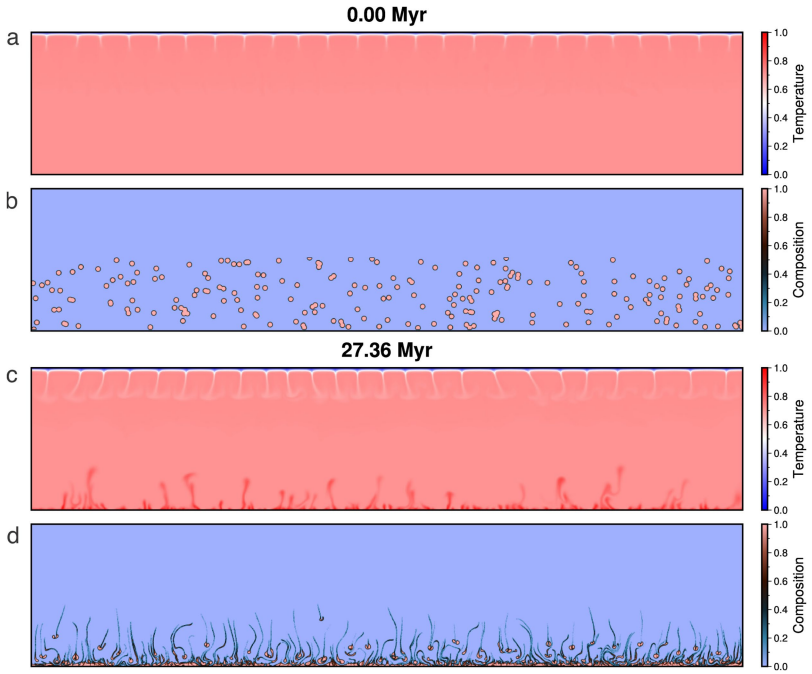

Extended Data Fig. 5 | One numerical experiment showing that dense TMM sinks to the CMB before upper mantle materials mix with lower mantle materials. a-d, Snapshots of the temperature fields (**a, c**) and compositional fields (**b, d**) at 0.00 Myr (**a-b**) and 27.36 Myr (**c-d**). At t = 0.00, random TMM blobs are placed in the lower mantle (**b**). After 27.36 Myr, the TMM blobs reach the CMB (**d**) whereas there is little mixing between the upper mantle and lower mantle (**c**).

Extended Data Table 1 | The depth of layer boundary and the enclosing mass of Theia mantle material below the boundary for the canonical Moon-forming giant impact simulations from ref. 19

Impact model	Depth of layer boundary (km)	Mass of Theia's mantle in lower layer ($M_\oplus$)
2	1,271	0.017
3	1,222	0.026
5	1,313	0.023
6	1,313	0.024
Average	1,280	0.023
1σ	43	0.0038

Here the layer boundary is defined by a compositional change, i.e., the fraction of TMM in the mantle[19]. We measure the fraction of enclosed mass below the layer boundary and then invert the enclosed mass radius relation in the PREM model[87] to get the depth of the layer boundary in present-day Earth.

Extended Data Table 2 | Results from the MFM simulations with updated versions of the ANEOS equations of state[16]

Run	Entropy boundary ($R_\oplus$)	Mass of TMM in lower layer ($M_\oplus$)	TMM solid fraction in lower layer (%)	Rheological boundary	Mass of TMM in lower layer ($M_\oplus$)	TMM solid fraction in lower layer (%)
1	0.85	0.016	8.2	0.74	0.0088	15
2	0.83	0.014	8.1	0.75	0.0084	5
3	0.81	0.013	11.	0.73	0.0082	16

The radius above which the mantle transit to a rheological liquid state (melt fraction >40%), the mass of TMM below that boundary, and the fractions of it that are solid. For comparison, we also listed the results using the boundary defined by entropy jump as in to ref. 19. These canonical impacts involve a low-mass (~0.12 M_E) Theia and a large proto-Earth (0.9 M_E) at ~45° impact angles, which are similar to ref. 19 but with enhanced resolution and an updated equation of state. The third MFM simulation has a particle count that is five times higher compared to the other two cases.

Extended Data Table 3 | Results from the SPH simulations

Run	Number of particles	Rheological boundary ($R_\oplus$)	Mass of TMM in lower layer ($M_\oplus$)	TMM solid fraction in lower layer (%)
1	10^5	0.779	3.88×10^{-5}	0.0
2	$10^{5.5}$	0.804	1.52×10^{-4}	0.0
3	10^6	0.811	4.62×10^{-4}	0.6
4	$10^{6.5}$	0.805	6.57×10^{-4}	0.3
5	10^7	0.805	1.17×10^{-3}	19.6
6	$10^{7.5}$	0.814	1.54×10^{-3}	31.1
7	10^8	0.823	2.59×10^{-3}	29.3

The radius above which the fraction of solid mantle material has dropped to 60%, the mass of TMM below that boundary, and the fraction of it that is solid, for different simulation resolutions.

Extended Data Table 4 | Major elemental compositions of the mantle of Theia and proto-Earth, and the bulk silicate Earth (BSE) (wt%) used in our thermodynamic modeling

Composition	SiO_2	Al_2O_3	FeO	MgO	CaO	Total
Theia_1	47.72	4.03	13.00	32.01	3.24	100.00
Theia_2	46.52	4.03	15.00	31.21	3.24	100.00
Theia_3	45.32	4.03	17.00	30.41	3.24	100.00
Proto-Earth	57.25	4.03	5.00	30.48	3.24	100.00
Bulk silicate Earth	47.95	4.03	7.79	36.98	3.24	100.00

The BSE composition is normalized to 100% from ref. 23.

Extended Data Table 5 | Physical parameters for mantle convection models

Parameter	Symbol	Value
Input Rayleigh number	Ra	1×10^{8}
Earth radius	R	6,371 km
Core–mantle boundary radius	r	3,503 km
Mantle thickness	h	2,868 km
Thermal expansivity	α_0	1×10^{-5}/K
Thermal diffusivity	κ_0	1×10^{-6} m^2/s
Gravitational acceleration	g_0	9.8 m/s^2
Temperature difference between surface and core-mantle boundary	ΔT	2,500 K
Background mantle reference density	ρ_0	3,300 kg/m^3
Reference viscosity	η_0	5.2×10^{21} Pa s

Extended Data Table 6 | Full list of performed mantle convection models

Case	Ra	Buoyancy number (density anomaly)	Activation energy	TMM Radius	Radioactive heating	Side boundary condition	Initial temperature
1 (REF)	1×10^8	1(2.5%)	9.21	50 km	0	Reflective	0.72
2	1×10^8	0.5(1.25%)	9.21	50 km	0	Reflective	0.72
3	1×10^8	1.4(3.5%)	9.21	50 km	0	Reflective	0.72
4	1×10^8	2(5.0%)	9.21	50 km	0	Reflective	0.72
5	1×10^8	1(2.5%)	9.21	25 km	0	Reflective	0.72
6	1×10^8	1(2.5%)	9.21	50 km	10	Reflective	0.72
7	1×10^8	1(2.5%)	11.51	50 km	0	Reflective	0.72
8	1×10^8	1(2.5%)	9.21	50 km	0	Periodic	0.72
9	1×10^8	1(2.5%)	9.21	50 km	0	Reflective	0.5

The radioactive heating rate in case 6 is a non-dimensional value for the TMM materials. The initial temperature is normalized by a reference temperature of 2,500 K.